



## Article

# Influence of the Facets of $\text{Bi}_{24}\text{O}_{31}\text{Br}_{10}$ Nanobelts and Nanosheets on Their Photocatalytic Properties

Qindan Zeng <sup>1,2</sup>, Wei Xie <sup>3</sup>, Zhihong Chen <sup>4</sup>, Xin Wang <sup>1,2,\*</sup> , Eser Metin Akinoglu <sup>2</sup> ,  
Guofu Zhou <sup>1,2</sup> and Lingling Shui <sup>1,5,\*</sup>

- <sup>1</sup> Guangdong Provincial Key Laboratory of Optical Information Materials and Technology & Institute of Electronic Paper Displays, South China Academy of Advanced Optoelectronics, South China Normal University, Guangzhou 510006, China; qindanzeng@m.scnu.edu.cn (Q.Z.); guofu.zhou@m.scnu.edu.cn (G.Z.)
- <sup>2</sup> International Academy of Optoelectronics at Zhaoqing, South China Normal University, Guangzhou 510006, China; e.akinoglu@zq-scnu.org
- <sup>3</sup> BTR NEW MATERIAL GROUP CO. LTD. Xitian High-tech Industrial Park, Guangming New District, Shenzhen 518106, China; xiewei@btrchina.com
- <sup>4</sup> Key Laboratory for Water Quality and Conservation of the Pearl River Delta, Ministry of Education, Institute of Environmental Research at Greater Bay, Guangzhou University, Guangzhou 510006, China; chenzhihong@gzhu.edu.cn
- <sup>5</sup> School of Information and Optoelectronic Science and Engineering, South China Normal University, Guangzhou 510006, China
- \* Correspondence: wangxin@scnu.edu.cn (X.W.); shuill@m.scnu.edu.cn (L.S.)

Received: 31 January 2020; Accepted: 14 February 2020; Published: 20 February 2020



**Abstract:**  $\text{Bi}_{24}\text{O}_{31}\text{Br}_{10}$  microcrystals composed of nanobelts and nanosheets with exposed (30-4) and (117) facets were synthesized by a simple hydrothermal method. The desired morphology and facets were obtained by adjusting the pH of the reaction system.  $\text{Bi}_{24}\text{O}_{31}\text{Br}_{10}$  nanobelts (BOB-NBs) with dominant (30-4) exposed facets were used for the photocatalytic degradation of tetracycline hydrochloride under visible light irradiation, with a degradation efficiency of up to 91% after 60 min of irradiation. The BOB-NBs possessed a higher charge separation and transfer efficiency, and showed less charge carrier recombination compared to the  $\text{Bi}_{24}\text{O}_{31}\text{Br}_{10}$  nanosheets (BOB-NSs), ascribed to a cooperative effect between the internal electric fields and surface active sites. A higher photocurrent response (2.6 times higher) was observed for BOB-NBs ( $12.8 \mu\text{A cm}^{-2}$ ) compared to that of BOB-NSs ( $4.9 \mu\text{A cm}^{-2}$ ). These findings are directional for a comprehensive understanding of the influence of the crystal facets of  $\text{Bi}_{24}\text{O}_{31}\text{Br}_{10}$  microcrystals on their photocatalytic activity and could help to guide the future design of high-performance photocatalytic materials.

**Keywords:**  $\text{Bi}_{24}\text{O}_{31}\text{Br}_{10}$  nanobelts;  $\text{Bi}_{24}\text{O}_{31}\text{Br}_{10}$  nanosheets; internal electric field; facet-dependent photocatalysis

## 1. Introduction

Crystal surface design is a good strategy to improve the photocatalytic performance of semiconductor materials. Photocatalysis is often related to the morphology and the specific exposed facets of a material, which in turn are linked to surface energy, electronic structure, and charge carrier dynamics [1–4]. For instance, Zhang et al. prepared  $\text{BiOCl}$  nanosheets (NSs) and noticed that the exposed (001) facets showed superior performance in pollutant photodegradation through direct semiconductor photoexcitation under ultraviolet light compared to a counterpart with exposed (010) facets [5]. Li et al. found that the (110) facets of  $\text{WO}_3$  nanowires possessed elevated photocatalytic oxidation activity compared to the (001) facets of  $\text{WO}_3$  NSs in a quantitative study of the influence of charge carrier dynamics on the photocatalytic activity [6]. Therefore, facet engineering can undoubtedly

influence photocatalysis and should be an exciting direction to pursue when searching for new, highly efficient photocatalytic materials.

$\text{Bi}_{24}\text{O}_{31}\text{Br}_{10}$  is considered a promising photocatalyst for pollutant degradation and hydrogen evolution reaction due to its unique properties, such as possessing a suitable energy band and superior chemical and optical stability [7–9]. Therefore, tremendous research efforts have been devoted to improving its photocatalytic activity. Some studies have demonstrated that the photocatalytic activity of  $\text{Bi}_{24}\text{O}_{31}\text{Br}_{10}$  can be further enhanced by doping it with other elements, for example  $\text{Bi}_{24}\text{O}_{31}\text{Cl}_x\text{Br}_{10-x}$  and Er-doped  $\text{Bi}_{24}\text{O}_{31}\text{Br}_{10}$  [10,11]. This could also be achieved by controlling the three-dimensional (3D) morphology and thickness of  $\text{Bi}_{24}\text{O}_{31}\text{Br}_{10}$  NSs [12–14], the construction of heterojunction architectures (such as in  $\text{BiOBr}/\text{Bi}_{24}\text{O}_{31}\text{Br}_{10}$ ,  $\text{Bi}_{12}\text{O}_{17}\text{Br}_2/\text{Bi}_{24}\text{O}_{31}\text{Br}_{10}$ , and  $\text{WO}_3/\text{Bi}_{24}\text{O}_{31}\text{Br}_{10}$ ) [15–17], and the synthesis of  $\text{Bi}_{24}\text{O}_{31}\text{Br}_{10}$  with oxygen and bromine vacancies or the formation of  $\text{Bi}_{24}\text{O}_{31}\text{Br}_{10}(\text{OH})$  [18–20].

An internal electric field is caused by the polarization of the nonuniform charge distribution between different constituent layers, which is favorable for the separation and transfer of photogenerated charge carriers. This is caused by the exposed facets and material composition, which lead to different charge distributions [5,21].  $\text{Bi}_{24}\text{O}_{31}\text{Br}_{10}$  is a layered structure made up of (Bi, O) and (Br) layers stacked together [22], which may induce the generation of internal electric fields. However, to the best of our knowledge, the internal electric field in different  $\text{Bi}_{24}\text{O}_{31}\text{Br}_{10}$  facet exposure and its effect on their photocatalytic activity has not yet been explored.

The hydrothermal synthesis method offers several advantages, including convenient manipulation, energy saving, and excellent control over size and morphology, etc. Therefore, numerous materials related to the above-mentioned nanomaterials have been successfully prepared by the hydrothermal method [23]. For instance, Li et al. obtained  $\text{WO}_3$  nanowires and NSs by hydrothermal synthesis [6]. Zhang and colleagues reported that the thickness of  $\text{Bi}_{24}\text{O}_{31}\text{Br}_{10}$  NSs could be controlled via hydrothermal synthesis [14].

Herein,  $\text{Bi}_{24}\text{O}_{31}\text{Br}_{10}$  nanobelts (NBs) with dominant (30-4) facets and NSs with dominant (117) facets were prepared by a simple hydrothermal process. The desired facets and morphology were achieved by adjusting the reaction parameters. The photocatalytic activities of the obtained materials were evaluated through the degradation of tetracycline hydrochloride (TTCH) under visible light, and the internal electric field and its impact on the photocatalytic performance of various exposed surfaces in terms of TTCH degradation was examined. The results indicated that  $\text{Bi}_{24}\text{O}_{31}\text{Br}_{10}$  nanobelts (BOB-NBs) with dominant (30-4) exposed facets exhibited a more favorable internal electric field to enhance the separation and transfer efficiency of photogenerated carriers, which is of benefit for improving the photocatalytic activity of TTCH degradation.

## 2. Results and discussion

### 2.1. Characterization

Both  $\text{Bi}_{24}\text{O}_{31}\text{Br}_{10}$  NBs and NSs were synthesized by a facile bottom-up hydrothermal process using  $\text{Bi}(\text{NO}_3)_3 \cdot 5\text{H}_2\text{O}$  and hexadecyl trimethyl ammonium bromide (CTAB) as Bi and Br sources, respectively. The desired facets and morphologies were obtained by adjusting the pH of the reaction system using NaOH to yield BOB-NSs and BOB-NBs at a pH of 10.6 and 10.0, respectively. Powder XRD patterns of BOB-NSs and BOB-NBs are shown in Figure 1. All the diffraction peaks were indexed to a phase of the monoclinic structure of  $\text{Bi}_{24}\text{O}_{31}\text{Br}_{10}$  with a space group of  $A2/m$ ,  $a = 1.0130$  nm,  $b = 0.4008$  nm, and  $c = 2.9970$  nm, and  $\beta = 90.15^\circ$  [22]. Moreover, no peaks corresponding to other phases are observed in Figure 1, indicating that the nanostructures are composed of single-phase  $\text{Bi}_{24}\text{O}_{31}\text{Br}_{10}$  with a high purity. However, some changes in intensity ratios were observed. The intensity ratios of the (30-4) and (117) peaks were recorded as 0.5 and 0.3 for BOB-NBs and BOB-NSs, respectively. In particular, the (30-4) peaks of the BOB-NBs appeared distinctly (see the red sign in Figure 1). Therefore, the BOB-NBs and BOB-NSs featured various crystallization orientations and exposed crystal facets.

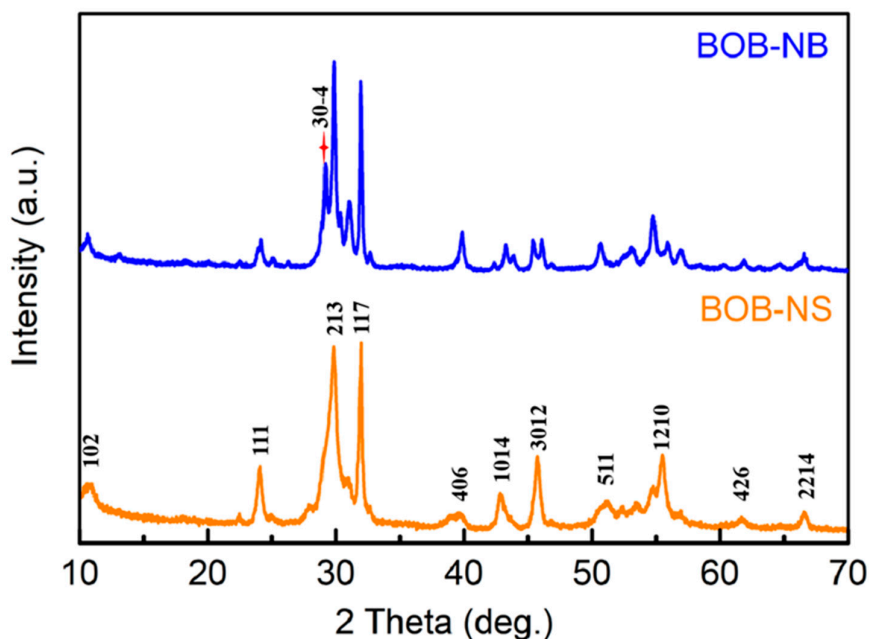


**Figure 1.** XRD patterns of  $\text{Bi}_{24}\text{O}_{31}\text{Br}_{10}$  nanobelts (BOB-NBs) and  $\text{Bi}_{24}\text{O}_{31}\text{Br}_{10}$  nanosheets (BOB-NSs).

SEM examination revealed that BOB-NSs consist of large-scale sheet-shaped structures with a width in the range of 0.5–2.0  $\mu\text{m}$  (Figure 2a). TEM imaging of an individual NS further confirmed the sheet-shaped structure (Figure 2b). Moreover, high-resolution TEM (HRTEM) imaging of individual  $\text{Bi}_{24}\text{O}_{31}\text{Br}_{10}$  NSs provided further insight into their structure (Figure 2c). The spacing between adjacent lattice planes of 0.28 nm was ascribed to the (117) facet [22]. The interfacial angle between the (117) and (1-17) planes was estimated to be  $89^\circ$ , as shown by the selected area electron diffraction patterns (SAED, Figure 2d), and is consistent with the theoretical value. Therefore, the (117) facet was identified as the main exposed facet of the BOB-NS.

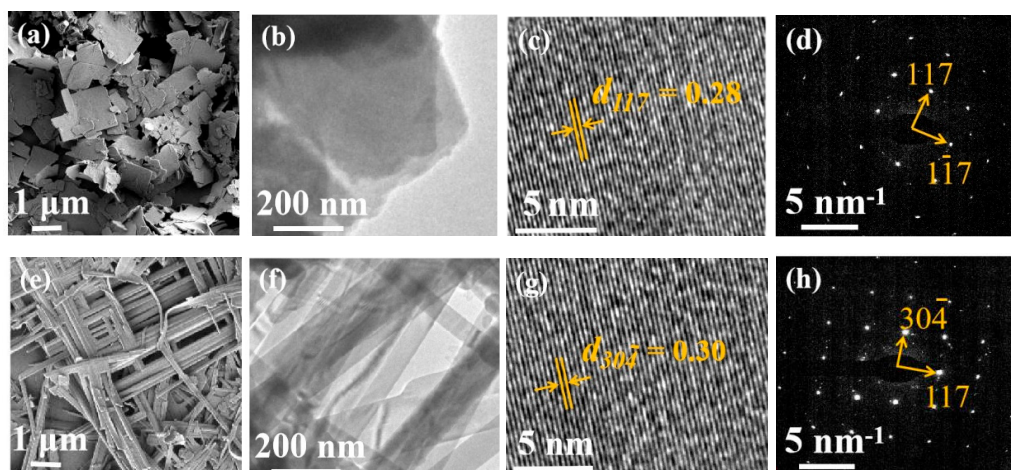


**Figure 2.** (a) and (e) SEM images of the BOB-NSs and BOB-NBs, (b) and (f) TEM images of the BOB-NSs and BOB-NBs, (c) and (g) high-resolution TEM (HRTEM) images of the BOB-NSs and BOB-NBs, (d) and (h) selected area electron diffraction (SAED) patterns of the BOB-NSs and BOB-NBs.

At a slightly lower pH (10.0) during synthesis, the as-prepared  $\text{Bi}_{24}\text{O}_{31}\text{Br}_{10}$  exhibited an NB morphology with a length and width in the range of 1–9  $\mu\text{m}$  and 50–250 nm, respectively (Figure 2e,f). The (30-4) facets with a lattice spacing of 0.30 nm can clearly be observed in Figure 2g [22]. The angle shown in the SAED pattern was recorded to be  $90.9^\circ$  (Figure 2h), which matches the calculated angle

value between the (30-4) and (117) planes. Therefore, the (30-4) facet was determined to be the main exposed facet in the BOB-NB and was in agreement with the XRD data.

Figure 3a shows the survey spectrum of XPS. The peaks for C, O, Bi, and Br are identified in the XPS survey spectrum. To calibrate the experimental data of the XPS test, the C 1s peak at 284.8 eV was set as the reference. The Bi 4f high-resolution XPS spectra exhibit the existence of two main peaks with binding energies at 159.1 eV and 164.4 eV (Figure 3b), corresponding to the Bi 4f<sub>7/2</sub> and Bi 4f<sub>5/2</sub> regions of Bi<sup>3+</sup>, respectively [24]. Figure 3c demonstrates that the O 1s XPS profile can be divided into two peaks with binding energies at 529.8 eV and 530.8 eV, belonging to lattice O in the (Bi<sub>2</sub>O<sub>2</sub>)<sup>2+</sup> layers of Bi<sub>24</sub>O<sub>31</sub>Br<sub>10</sub> and oxygen atoms in O–H groups, respectively [25,26]. The Br 3d XPS spectrum can also be divided into two peaks with binding energies at 68.2 and 69.1 eV, which are attributed to the characteristic signals of Br 3d<sub>5/2</sub> and Br 3d<sub>3/2</sub> of Br<sup>−</sup>, respectively [17] (Figure 3d). Notably, the Br 3d peaks of BOB-NBs exhibited a small rightward shift of about 0.07 eV compared to those of BOB-NSs, indicating a slight difference in the surface compositions of BOB-NBs and BOB-NSs. These results are in agreement with the above-mentioned XRD results.

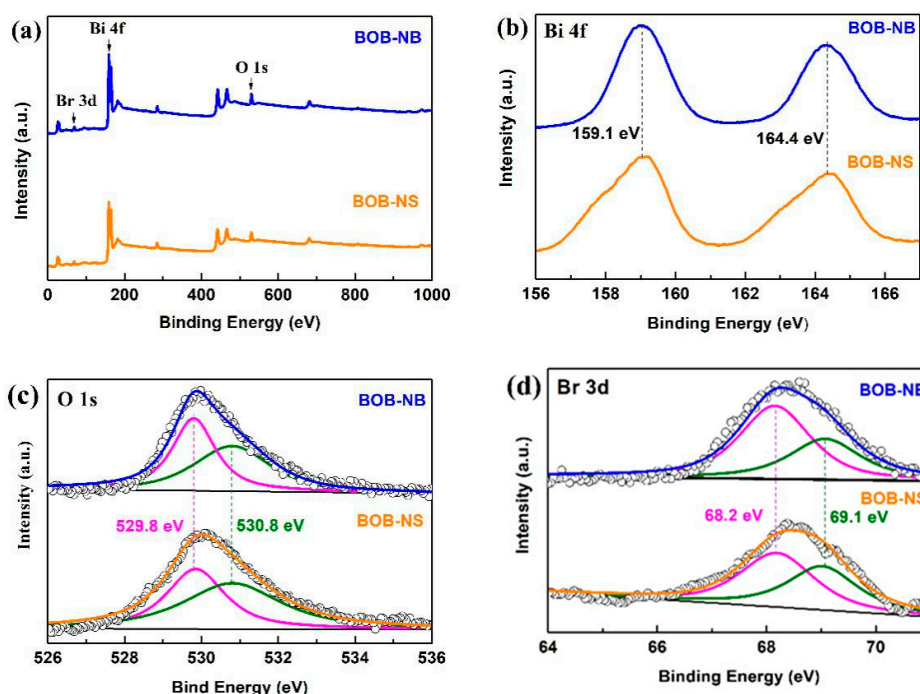


**Figure 3.** (a) Survey XPS spectrum, (b) Bi 4f, (c) O1s, and (d) Br 3d of the BOB-NBs and BOB-NSs.

## 2.2. Photocatalytic Properties regarding TTCH Degradation

The photocatalytic oxidation performance of BOB-NBs and BOB-NSs was evaluated through the degradation of TTCH (Figure 4). BiOBr was used as a reference to compare the data. In the absence of the photocatalysts, TTCH did not show any degradation with or without irradiation. The adsorption–desorption equilibria of the as-prepared samples were reached within 30 min in the dark. The adsorption ability of BOB-NBs was similar to that of BOB-NSs. Under visible-light irradiation, both samples performed well but the BOB-NB illustrated the best TTCH degradation performance, with up to 91% transformed TTCH during 60 min of visible-light irradiation. The catalytic performance of the BOB-NS was slightly lower with 81% TTCH degradation, while BiOBr reached only 73% (Figure 4a).

The reactant concentration was low (20 mg L<sup>−1</sup> TTCH); therefore, the kinetic constant *k* of TTCH degradation was obtained by using the following pseudo first-order Equation (1) [14]:

The kinetic constant *k* of TTCH degradation was obtained by Equation (1):

$$-\ln(C_t/C_0) = kt \quad (1)$$



where  $k$  is the apparent kinetic rate constant, and  $C_0$  and  $C_t$  are the concentrations of TTCH initially and at the given time  $t$ , respectively.

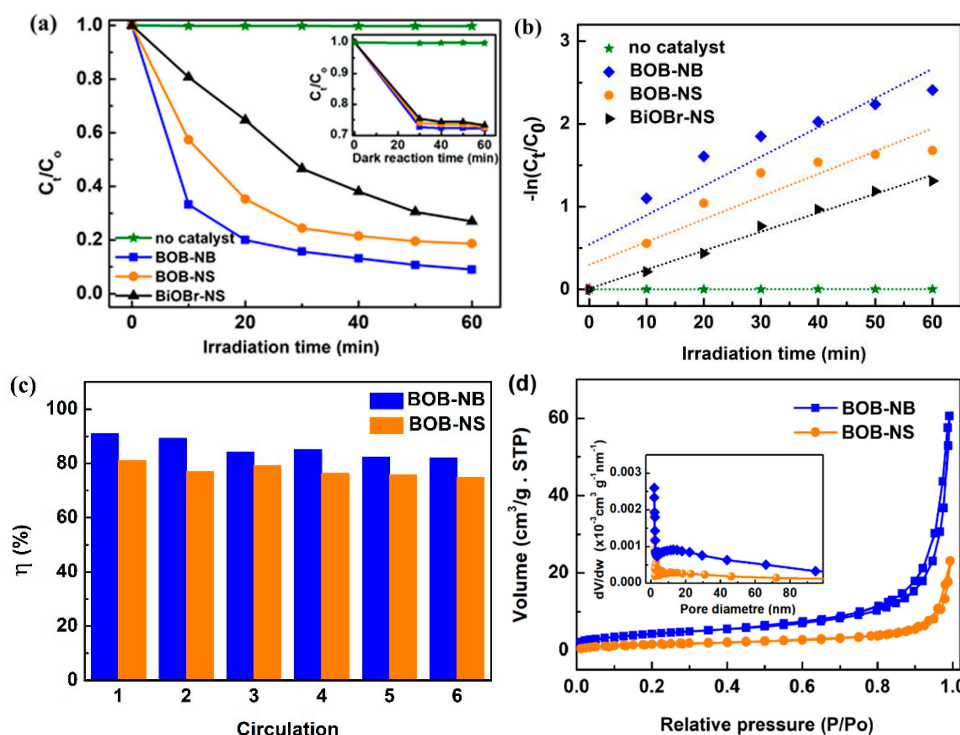


**Figure 4.** (a) Photocatalytic degradation of tetracycline hydrochloride (TTCH) with different photocatalysts (insert image shows the dark reaction), (b) corresponding kinetic equations obtained within 60 min, (c) recycling properties of the photocatalytic TTCH degradation over the BOB-NBs and BOB-NSs under the same conditions, and (d) the  $N_2$  adsorption–desorption isotherms and the pore distribution curves of the BOB-NSs and BOB-NBs.

The  $k$  values of BOB-NBs, BOB-NSs, and BiOBr after 60 min of TTCH degradation were calculated as  $0.035 \text{ min}^{-1}$ ,  $0.027 \text{ min}^{-1}$ , and  $0.022 \text{ min}^{-1}$ , respectively (Figure 4b). The kinetic rate constant  $k$  of BOB-NBs was 1.3 times larger than that of BOB-NSs, and 1.6 times larger than that of BiOBr. Therefore, BOB-NBs showed the best photocatalytic properties. Both BOB-NBs and BOB-NSs possessed good stability and reusability under the same conditions (Figure 4c). This demonstrated that both BOB-NBs and BOB-NSs could be used as potential candidates for photocatalytic applications.

The Brunauer–Emmett–Teller (BET) surface areas were measured, and those of BOB-NBs and BOB-NSs were  $15.80 \text{ m}^2 \text{ g}^{-1}$  and  $6.02 \text{ m}^2 \text{ g}^{-1}$ , respectively (Figure 4d). This indicated that a higher photocatalytic activity for BOB-NBs could be partly attributed to their surface area.  $N_2$  adsorption–desorption isotherms and pore size distribution were explored to reveal the porosity of the synthesized products. The  $N_2$  adsorption–desorption isotherm of BOB-NBs presents a type-IV isotherm plot with a typical H3 hysteresis loop, indicating a hierarchical pore structure consisting of meso- and macro-porosity. The above analysis was also supported by the pore size distribution, which showed distinct peaks at  $\sim 2.5 \text{ nm}$  and  $\sim 15 \text{ nm}$ .

### 2.3. Band structures of BOB-NSs and BOB-NBs

The optical properties of the as-prepared samples were examined by the ultraviolet-visible (UV-vis) diffuse reflectance spectra (DRS). From the results, the absorption edges of BOB-NBs and BOB-NSs indicate that BOB-NBs have a slightly narrower band gap (Figure 5a) [27]. Notably, the light absorption of BOB-NBs was slightly higher compared to that of BOB-NSs.

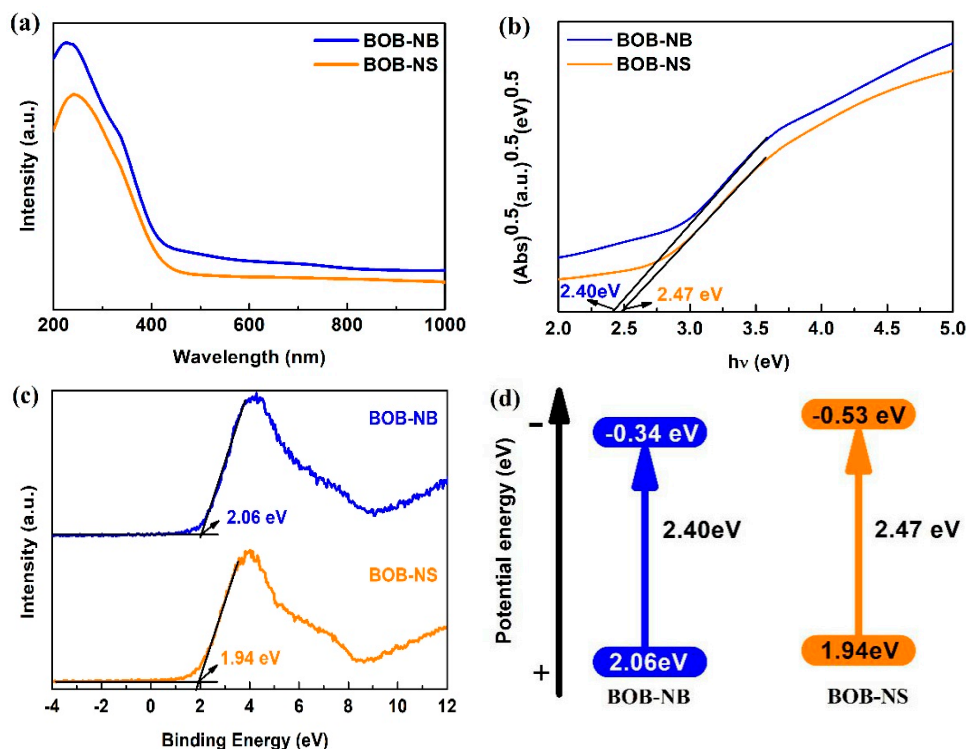


**Figure 5.** (a) UV-vis DRS graph, (b) band gap values, (c) XPS valence band spectrum, and (d) energy band structure of BOB-NSs and BOB-NBs.

The band gap values were calculated from Kubelka-Munk (KM) processed UV-vis spectra. Figure 5b shows that the values for BOB-NBs and BOB-NSs are 2.40 eV and 2.47 eV, respectively. To calculate the relative band structures of BOB-NBs and BOB-NSs, the valence band maximum (VBM) potential was obtained by XPS measurement of the valence band, and the results revealed that the VBM of BOB-NBs and BOB-NSs was 2.06 eV and 1.94 eV, respectively (Figure 5c). Accordingly, the values of conduction band minimum (CBM) potential of BOB-NBs and BOB-NSs were recorded as -0.34 eV and -0.53 eV, respectively. The entire energy band structure is illustrated in Figure 5d. Compared to BOB-NSs, BOB-NBs exhibited a slightly more positive VBM potential, indicating that BOB-NBs might exhibit a slightly stronger oxidizing ability than BOB-NSs.

#### 2.4. Investigation of the photocatalytic mechanism

To gain a better understanding of the differences in the as-prepared samples, the crystal structures were further analyzed. With respect to BiOBr,  $Bi_{24}O_{31}Br_{10}$  has a layered crystal structure characterized by stair-like (Bi, O) slabs and (Br) slabs stacked together with nonbonding interactions through Br atoms along the [30-4]-axis to form a unique layered structure [22] (Figure 6a). Ascribed to an inhomogeneous charge distribution between (Bi, O) slabs and (Br) slabs, the internal electric field would be induced in the bulk of  $Bi_{24}O_{31}Br_{10}$  along the [30-4] direction, enabling the effective separation of photoinduced electrons and holes. The elevated magnitude of the internal electric field led to better effective charge separation. Therefore, density functional theory (DFT) calculations were used to assess the charge density distribution on the exposed (30-4) and (117) facets along the crystal *c* direction. The average charge densities of (30-4) were recorded as 0.43 and -0.38 for (Bi, O) and (Br) layers, respectively. Comparative analysis indicates that the average charge densities of the (117) facets were estimated to be 0.22 and -0.35 for (Bi, O) and (Br) layers, respectively. Moreover, the internal electric field along the (30-4) orientation was perpendicular to the (30-4) facet in BOB-NBs, but approximately parallel to the (117) facet in BOB-NSs (Figure 6b). Therefore, the magnitude of the internal electric field of the

(30-4) facet was higher than that of the (117) facet, indicating that charge carrier separation and transfer driven by the internal electric field were more favorable in BOB-NBs with exposed (30-4) facets.

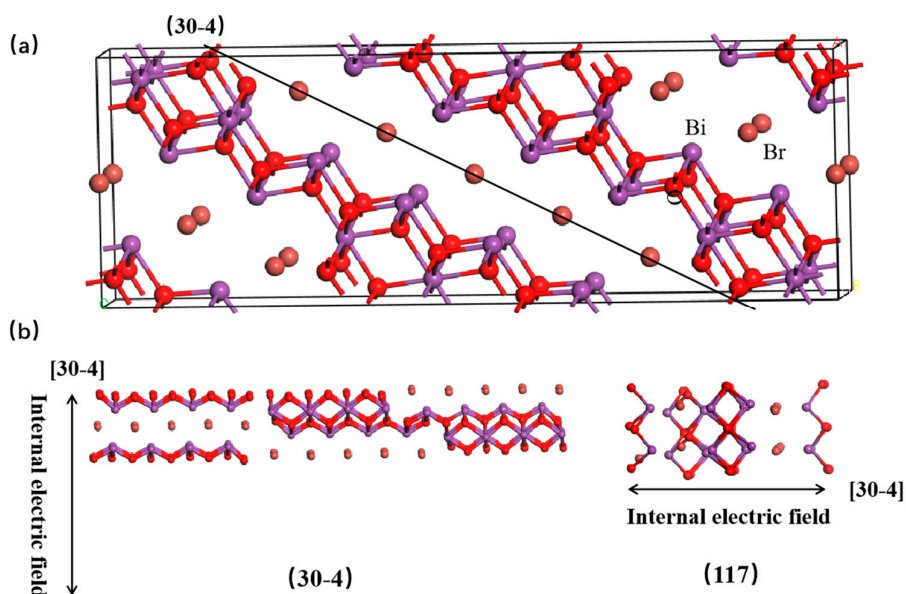


**Figure 6.** (a) Crystal structure of  $\text{Bi}_{24}\text{O}_{31}\text{Br}_{10}$ , (b) model showing the direction of the internal electric field of  $\text{Bi}_{24}\text{O}_{31}\text{Br}_{10}$  with (30-4) exposed facets and (117) exposed facets.

The above-mentioned data were further confirmed by photo-response measurements. Notably, the intensity of the photocurrent was proportional to the charge carrier density. The highest photocurrent response for BOB-NBs was estimated to be 2.6-fold compared to that for BOB-NSs (Figure 7a). Mott-Schottky plots depicted slopes inversely proportional to the density of the charge carriers (Figure 7b). The charge carrier density of BOB-NBs was 1.8-fold higher than that of BOB-NSs. Thus, the photocatalytic separation efficiency of BOB-NBs was 1.4-fold higher than that of BOB-NSs. Moreover, the Nyquist plot analysis shows a reduced diameter for BOB-NBs compared to that of BOB-NSs (Figure 7c), indicating a superior charge transfer efficiency in BOB-NBs. Thus, the charge carrier separation and transfer in BOB-NBs are superior to those in BOB-NSs.

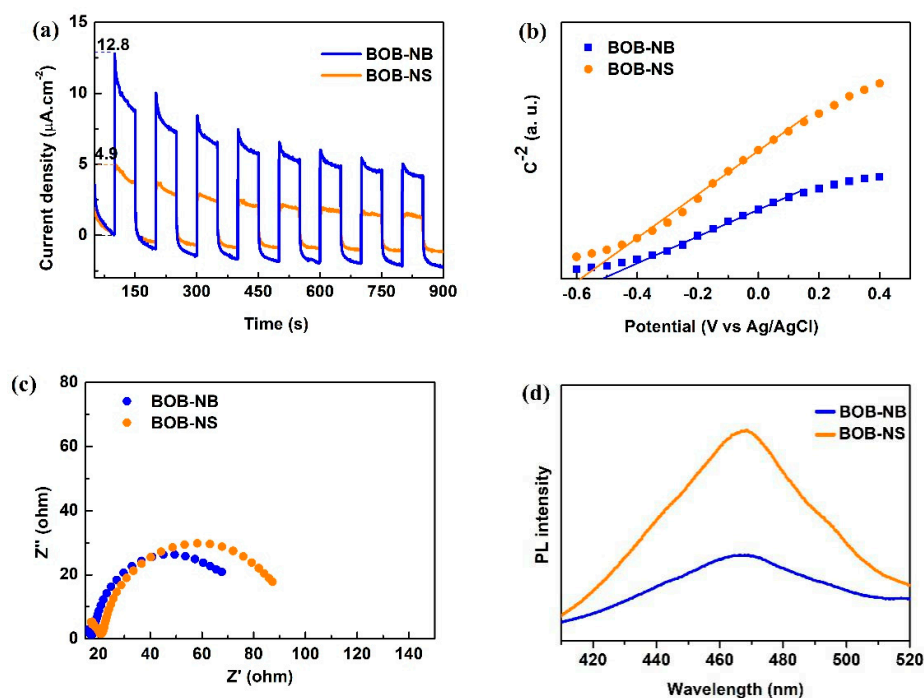


**Figure 7.** (a) Photocurrent response, (b) Mott-Schottky plots, (c) electrochemical impedance spectroscopy (EIS) Nyquist plots, and (d) photoluminescence (PL) spectra of BOB-NSs and BOB-NBs.

The photoinduced electrons (or holes) can recombine through hole trapping (or electron trapping). The recombination rates of photoinduced electron–hole pairs were investigated by photoluminescence (PL) spectra. Figure 7d exhibits the presence of emission peaks at 469 nm under 290 nm UV light excitation. The weaker PL intensity of BOB-NBs implies a lower recombination rate of photogenerated electrons and holes. Therefore, BOB-NBs with exposed (30-4) facets appear to exhibit a better efficiency for charge carrier separation. In addition, compared to BOB-NSs, BOB-NBs show advantages such as a larger specific surface area, a slightly stronger oxidizing ability, and a stronger internal electric field, which are beneficial for photocatalysis.

Based on these aforementioned results, a mechanism was proposed as follows. First, under visible light irradiation, both BOB-NBs and BOB-NSs absorbed visible light because of their suitable band gap. Then, the separation of photoelectron and photohole pairs and diffusion took place. The internal electric field between (Bi, O) slabs and (Br) slabs enabled the effective separation of the photoinduced electrons and holes along the [30–4] direction. The internal electric fields were perpendicular to the  $\text{Bi}_{24}\text{O}_{31}\text{Br}_{10}$ -(30-4) microsheets, but approximately parallel to those of  $\text{Bi}_{24}\text{O}_{31}\text{Br}_{10}$ -(117). Consequently, charge separation and transfer were more favorable in  $\text{Bi}_{24}\text{O}_{31}\text{Br}_{10}$ -(30-4) assisted by internal electric fields. Furthermore, BOB-NBs showed more active sites, as indicated by a larger BET surface area compared to BOB-NSs. More electrons and holes could be captured by these active sites, which promoted the surface charge separation [5]. Therefore, a cooperative effect between the internal electric fields along the [30–4] direction and the surface active sites would further improve the charge carrier separation and transfer efficiency of photogenerated electrons and holes, leading to the superior photocatalytic performance of  $\text{Bi}_{24}\text{O}_{31}\text{Br}_{10}$ -(30-4). Thus, BOB-NBs possessed more  $\text{h}^+$  and active species participating in the degradation of TTCH.



### 3. Materials and Methods

#### 3.1. Synthesis of BOB-NSs and BOB-NBs

To prepare the  $\text{Bi}_{24}\text{O}_{31}\text{Br}_{10}$  nanosheets (BOB-NSs),  $\text{Bi}(\text{NO}_3)_3 \cdot 5\text{H}_2\text{O}$  (1.0 g) and CTAB (1.0 g) were dissolved in deionized water (50 mL) at room temperature with stirring. NaOH (1 M) solution was added to adjust the pH value to 10.6. Subsequently, the solution was sealed in a 100 mL Teflon-lined stainless-steel reactor and heated at 180 °C for 15 h. The obtained precipitates were collected and rinsed with ethanol and deionized water, and finally dried in a vacuum oven at 80 °C.

$\text{Bi}_{24}\text{O}_{31}\text{Br}_{10}$  nanobelts (BOB-NBs) were prepared by a similar procedure, except the pH value was 10. Next, hydrothermal treatment of the final solutions was carried out under the same experimental conditions.

#### 3.2. Characterization

X-ray diffraction (XRD, Bruker D8A) was used for analyzing the phase structures of  $\text{Bi}_{24}\text{O}_{31}\text{Br}_{10}$ . The microstructure and morphology of  $\text{Bi}_{24}\text{O}_{31}\text{Br}_{10}$  were viewed by scanning electron microscopy (SEM, ZEISS Gemini 50, Germany). Transmission electron microscopy (TEM) and high-resolution TEM (HRTEM) measurements were carried out using a FEI Talos F200X microscope at a working voltage of 200 kV. X-ray photoelectron spectroscopy (XPS, PHI Quattro SXM) was used for surface analysis. The optical properties were measured by UV-vis diffraction reflectance spectroscopy (DRS, METASH UV-8000A, SHJH Group Company, Shanghai, China). Brunauer-Emmett-Teller (BET) specific surface areas of samples were characterized by nitrogen adsorption-desorption measurements (USA, Micromeritics ASAP 2460). Photoluminescence (PL) emission spectroscopy was conducted using a fluorescence spectrophotometer (F-4600 Hitachi, Japan).

#### 3.3. Photocatalytic Tests

The photocatalytic activity experiments were performed in a multichannel photochemical reaction system composed of nine reaction positions (PCX50C Discover, Beijing Perfectlight Technology Co., Ltd., Beijing, China). A white light emitting diode (LED) lamp (10 W) was employed as a light source. The radiation flux was determined using a digital radiometer and was estimated to be approximately  $100 \text{ mW cm}^{-2}$ . All experiments were carried out simultaneously by dispersing photocatalyst powder (50 mg) in aqueous solution (50 mL) containing TTCH ( $20 \text{ mg L}^{-1}$ ). Prior to the photocatalytic degradation tests, each mixture was stirred without light for 60 min in order to ensure sufficient adsorption-desorption equilibrium. During illumination, suspensions (3 mL) were taken out at given time intervals under visible light irradiation followed by centrifugation separation to obtain the supernatants. The residual concentration of TTCH was monitored by UV-vis spectrophotometry.

#### 3.4. Photoelectrochemical Measurements

The photocurrent response, electrochemical impedance spectroscopy (EIS), and Mott-Schottky profiles were conducted by an electrochemical workstation in a three-electrode cell, where Pt was the counter electrode and Ag/AgCl was the reference electrode. All photoelectrochemical experiments were performed in 0.5 M  $\text{Na}_2\text{SO}_4$  aqueous electrolyte. The working photoelectrodes (size  $10 \times 10 \text{ mm}^{-2}$ ) were prepared by coating aqueous slurries of the samples on the fluorine-doped tin oxide (FTO) glass substrates. Aqueous slurries of the samples were obtained by grinding each sample (25 mg) with poly(3,4-ethylenedioxythiophene)-poly(styrenesulfonate) (PEDOT-PSS) aqueous solution (80  $\mu\text{L}$ ) and water (150  $\mu\text{L}$ ). The resulting films were annealed in a furnace at 150 °C for 10 min.

A bias voltage (0.612V) was applied to measure the photoresponse by shutting out the light. The EIS measurements were characterized in a frequency range from 0.01 Hz to 1000 kHz, at an amplitude of 5 mV. The Mott-Schottky plots were used to evaluate the flat band potential at a frequency of 1 kHz and an applied voltage from -0.6 to 0.6 V. A solar simulator with an AM1.5 filter was utilized as the light source.

### 3.5. Density Functional Theory (DFT) Calculations

All the DFT calculations were implemented in the Vienna Ab initio Simulation Package (VASP5.4) [28,29] via the generalized gradient approximation (GGA), Perdew-Burke-Ernzerhof (PBE) exchange-correlation potential [30,31]. A Monkhorst-Pack mesh of  $7 \times 1 \times 1$  was chosen for  $\text{Bi}_{24}\text{O}_{31}\text{Br}_{10}$  NBs with exposed (30-4) facets, and one of  $2 \times 1 \times 1$  was used for  $\text{Bi}_{24}\text{O}_{31}\text{Br}_{10}$  NSs with exposed (117) facets. The cut-off energy was set at 400 eV, and the convergence criterion for energy was chosen as  $1 \times 10^{-4}$  eV/cell. The Gaussian smearing method was employed for accurate calculation of the electronic structures.

## 4. Conclusions

In summary, BOB-NBs and BOB-NSs with respective dominant facets of (30-4) and (117) were prepared by a facile hydrothermal method. Compared to BOB-NSs, BOB-NBs featured more efficient bulk charge carrier separation and promoted charge carrier transfer on the surface and the interface due to the synergistic effect and cooperative effect of the internal electric fields and surface active sites. Thus, the BOB-NBs with dominant (30-4) exposed facets show a superior photocatalytic activity regarding the degradation of TTCH under visible light. This study offers a new strategy for the design of high-performance photocatalytic materials.

**Author Contributions:** Q.Z., X.W., and L.S. designed the project; Q.Z. and X.W. performed the experiments related to the project and wrote the paper; W.X. carried out the DFT calculations and mechanistic study. All authors have read and agreed to the published version of the manuscript.

**Funding:** The authors greatly acknowledge the financial support from the National Natural Science Foundation of China Program (No. 51602111), Xijiang R&D Team (X.W.), Guangdong Innovative and Entrepreneurial Team Program (No. 2016ZT06C517), Special Fund Project of Science and Technology Application in Guangdong (2017B020240002), Science and Technology Program of Guangzhou (2019050001), and the National 111 project.

**Conflicts of Interest:** The authors declare no conflict of interest.

## References

1. Lan, L.; Li, Y.Z.; Zeng, M.; Mao, M.Y.; Ren, L.; Yang, Y.; Liu, H.H.; Yun, L.; Zhao, X.J. Efficient UV-vis-infrared light-driven catalytic abatement of benzene on amorphous manganese oxide supported on anatase  $\text{TiO}_2$  nanosheet with dominant 001 facets promoted by a photothermocatalytic synergetic effect. *Appl. Catal. B Environ.* **2017**, *203*, 494–504. [\[CrossRef\]](#)
2. Zhang, L.; Wang, W.Z.; Sun, S.M.; Jiang, D.; Gao, E.P. Selective transport of electron and hole among 001 and 110 facets of  $\text{BiOCl}$  for pure water splitting. *Appl. Catal. B Environ.* **2015**, *162*, 470–474. [\[CrossRef\]](#)
3. Li, M.; Zhang, Y.H.; Li, X.W.; Yu, S.X.; Du, X.; Guo, Y.X.; Huang, H.W. In-depth insight into facet-dependent charge movement behaviors and photo-redox catalysis: A case of {0 0 1} and {0 1 0} facets  $\text{BiOCl}$ . *J. Colloid Interface Sci.* **2017**, *508*, 174–183. [\[CrossRef\]](#)
4. Li, H.; Shang, J.; Shi, J.G.; Zhao, K.; Zhang, L.Z. Facet-dependent solar ammonia synthesis of  $\text{BiOCl}$  nanosheets via a proton-assisted electron transfer pathway. *Nanoscale* **2016**, *8*, 1986–1993. [\[CrossRef\]](#)
5. Jiang, J.; Zhao, K.; Xiao, X.Y.; Zhang, L.Z. Synthesis and Facet-Dependent Photoreactivity of  $\text{BiOCl}$  Single Crystalline Nanosheets. *J. Am. Chem. Soc.* **2012**, *134*, 4473–4476. [\[CrossRef\]](#)
6. Lin, R.; Wan, J.W.; Xiong, Y.; Wu, K.L.; Cheng, W.C.; Zhou, G.; Wang, D.S.; Peng, Q.; Chen, C.; Li, Y.D. A quantitative study of charge carrier dynamics in well-defined  $\text{WO}_3$  nanowires and nanosheets: Insight into the crystal facet effect in photocatalysis. *J. Am. Chem. Soc.* **2018**, *140*, 9078–9082. [\[CrossRef\]](#)
7. Shang, J.; Hao, W.C.; Lv, X.J.; Wang, T.M.; Wang, X.L.; Du, Y.; Dou, S.X.; Xie, T.F.; Wang, D.J.; Wang, J.O. Bismuth Oxybromide with Reasonable Photocatalytic Reduction Activity under Visible Light. *ACS Catal.* **2014**, *4*, 954–961. [\[CrossRef\]](#)
8. Xiao, X.; Liu, C.L.; Hu, R.P.; Zuo, X.X.; Nan, J.M.; Li, L.S.; Wang, L.S. Oxygen-rich bismuth oxyhalides: Generalized one-pot synthesis, band structures and visible-light photocatalytic properties. *J. Mater. Chem.* **2012**, *22*, 22840–22843. [\[CrossRef\]](#)

9. Song, J.; Zhang, L.; Yang, J.; Huang, X.H.; Hu, J.S. Hierarchical porous Bi<sub>24</sub>O<sub>31</sub>Br<sub>10</sub> microarchitectures assembled by ultrathin nanosheets with strong adsorption and excellent photocatalytic performances. *Mater. Des.* **2017**, *123*, 128–136. [\[CrossRef\]](#)
10. Liu, Z.S.; Niu, J.N.; Feng, P.Z.; Zhu, Y.B. Solvothermal synthesis of Bi<sub>24</sub>O<sub>31</sub>Cl<sub>x</sub>Br<sub>10-x</sub>, solid solutions with enhanced visible light photocatalytic property. *Ceram. Int.* **2014**, *41*, 4608–4615. [\[CrossRef\]](#)
11. Liu, Z.S.; Liu, Z.L.; Liu, J.L.; Zhang, J.W.; Zhou, T.F.; Ji, X. Enhanced photocatalytic performance of Er-doped Bi<sub>24</sub>O<sub>31</sub>Br<sub>10</sub>: Facile synthesis and photocatalytic mechanism. *Mater. Res. Bull.* **2016**, *76*, 256–263. [\[CrossRef\]](#)
12. Deng, H.; Wang, J.W.; Peng, Q.; Wang, X.; Li, Y.L. Controlled hydrothermal synthesis of bismuth oxyhalide nanobelts and nanotubes. *Chem. Eur. J.* **2005**, *22*, 6519–6524. [\[CrossRef\]](#) [\[PubMed\]](#)
13. Wang, C.Y.; Zhang, X.; Zhang, Y.J.; Chen, J.J.; Huang, G.X.; Jiang, J.; Wang, W.K.; Yu, H.Q. Direct generation of hydroxyl radicals over bismuth oxybromide nanobelts with tuned band structure for photocatalytic pollutant degradation under visible light irradiation. *Appl. Catal. B Environ.* **2018**, *237*, 464–472. [\[CrossRef\]](#)
14. Wang, C.Y.; Zhang, X.; Qiu, H.B.; Huang, G.X.; Yu, H.Q. Bi<sub>24</sub>O<sub>31</sub>Br<sub>10</sub> nanosheets with controllable thickness for visible-light-driven catalytic degradation of tetracycline hydrochloride. *Appl. Catal. B Environ.* **2017**, *205*, 615–623. [\[CrossRef\]](#)
15. Wu, W.; Ma, X.D.; Li, D.; Xuan, Y.W.; Meng, S.C.; Chen, M. Assembly of WO<sub>3</sub> nanosheets/Bi<sub>24</sub>O<sub>31</sub>Br<sub>10</sub> nanosheets composites with superior photocatalytic activity for degradation of tetracycline hydrochloride. *J. Mater. Sci.* **2018**, *53*, 15804–15816. [\[CrossRef\]](#)
16. Li, F.T.; Wang, Q.; Ran, J.R.; Hao, Y.J.; Wang, X.J.; Zhao, D.S.; Qiao, S.Z. Ionic liquid self-combustion synthesis of BiOBr/Bi<sub>24</sub>O<sub>31</sub>Br<sub>10</sub> heterojunctions with exceptional visible-light photocatalytic performances. *Nanoscale* **2015**, *7*, 1116–1126. [\[CrossRef\]](#)
17. Peng, Y.; Yu, P.P.; Chen, Q.G.; Zhou, H.Y.; Xu, A.W. Facile Fabrication of Bi<sub>12</sub>O<sub>17</sub>Br<sub>2</sub>/Bi<sub>24</sub>O<sub>31</sub>Br<sub>10</sub> Type II heterostructures with high visible photocatalytic activity. *J. Phys. Chem. C* **2015**, *119*, 13032–13040. [\[CrossRef\]](#)
18. Xiao, X.; Zheng, C.X.; Lu, M.L.; Zhang, L.; Liu, F.; Zuo, X.X.; Nan, J.M. Deficient Bi<sub>24</sub>O<sub>31</sub>Br<sub>10</sub> as a highly efficient photocatalyst for selective oxidation of benzyl alcohol into benzaldehyde under blue LED irradiation. *Appl. Catal. B: Environ.* **2017**, *228*, 142–151. [\[CrossRef\]](#)
19. Xiao, B.; Zhao, W.H.; Xiang, Y.B.; Wu, X.Y.; Zhang, G.K. Vis-NIR responsive Bi<sub>24</sub>O<sub>31</sub>Br<sub>10</sub> and corresponding composite with up-conversion phosphor towards efficient photocatalytic oxidation. *Appl. Surf. Sci.* **2019**, *489*, 210–219. [\[CrossRef\]](#)
20. Dai, Y.T.; Li, C.; Shen, Y.B.; Zhu, S.J.; Hvid, M.S.; Wu, L.C.; Skibsted, J.; Li, Y.W.; Niemantsverdriet, J.W.H.; Besenbacher, F.; et al. Efficient Solar Driven Hydrogen Transfer by Bismuth Based Photocatalyst with Engineered Basic Sites. *J. Am. Chem. Soc.* **2019**, *58*, 6265–6270. [\[CrossRef\]](#)
21. Li, J.; Cai, L.J.; Shang, J.; Yu, Y.; Zhang, L.Z. Giant Enhancement of Internal Electric Field Boosting Bulk Charge Separation for Photocatalysis. *Adv. Mater.* **2016**, *28*, 4059–4064. [\[CrossRef\]](#) [\[PubMed\]](#)
22. Eggenweiler, U.; Keller, E.; Krammer, V. Redetermination of the crystal structures of the ‘Arppe compound’ Bi<sub>24</sub>O<sub>31</sub>Cl<sub>10</sub> and the isomorphous Bi<sub>24</sub>O<sub>31</sub>Br<sub>10</sub>. *Acta Cryst.* **2000**, *56*, 431–437. [\[CrossRef\]](#) [\[PubMed\]](#)
23. Shi, W.D.; Song, S.Y.; Zhang, H.J. Hydrothermal synthetic strategies of inorganic semiconducting nanostructures. *Chem. Soc. Rev.* **2013**, *42*, 5714–5743. [\[CrossRef\]](#)
24. Wang, C.Y.; Zhang, X.; Song, X.N.; Wang, W.K.; Yu, H.Q. Novel Bi<sub>12</sub>O<sub>15</sub>Cl<sub>6</sub> Photocatalyst for the Degradation of Bisphenol A under Visible-Light Irradiation. *ACS Appl. Mater. Interfaces* **2016**, *8*, 5320–5326. [\[CrossRef\]](#)
25. Zhang, N.; Li, X.Y.; Ye, H.C.; Chen, S.M.; Ju, H.X.; Liu, D.B.; Lin, Y.; Ye, W.; Wang, C.M.; Xu, Q.; et al. Oxide Defect Engineering Enables to Couple Solar Energy into Oxygen Activation. *J. Am. Chem. Soc.* **2016**, *138*, 8928–8935. [\[CrossRef\]](#)
26. Wang, H.; Yong, D.Y.; Chen, S.C.; Jiang, S.L.; Zhang, X.D.; Shao, W.; Zhang, Q.; Yan, W.S.; Pan, B.C.; Xie, Y. Oxygen-Vacancy-Mediated Exciton Dissociation in BiOBr for Boosting Charge-Carrier-Involved Molecular Oxygen Activation. *J. Am. Chem. Soc.* **2018**, *140*, 1760–1766. [\[CrossRef\]](#)
27. Li, Q.; Rellán-Piñero, M.; Almora-Barrios, N.; Garcia-Ratés, M.; Remediakis, I.N.; López, N. Shape Control in Concave Metal Nanoparticles by Etching. *Nanoscale* **2017**, *9*, 13089–13094. [\[CrossRef\]](#)
28. Kresse, G.; Furthmüller, J. Efficiency of ab-initio total energy calculations for metals and semiconductors using a plane-wave basis set. *Comput. Mater. Sci.* **1996**, *6*, 15–50. [\[CrossRef\]](#)
29. Kresse, G.; Furthmüller, J. Efficient iterative schemes for ab initio total-energy calculations using a plane-wave basis set. *Phys. Rev. B* **1996**, *54*, 11169–11186. [\[CrossRef\]](#)

30. Perdew, J.P.; Burke, K.; Ernzerhof, M. Generalized gradient approximation made simple. *Phys. Rev. Lett.* **1996**, *77*, 3865–3868. [[CrossRef](#)]
31. Grimme, S.; Ehrlich, S.; Goerigk, L. Effect of the damping function in dispersion corrected density functional theory. *J. Comput. Chem.* **2011**, *32*, 1456–1465. [[CrossRef](#)] [[PubMed](#)]



© 2020 by the authors. Licensee MDPI, Basel, Switzerland. This article is an open access article distributed under the terms and conditions of the Creative Commons Attribution (CC BY) license (<http://creativecommons.org/licenses/by/4.0/>).